Journal of Power Sources 195 (2010) 1522–1528

Contents lists available at ScienceDirect

Journal of Power Sources

journal homepage: www.elsevier.com/locate/jpowsour

Short communication

Facile synthesis and electrochemical properties of conducting $SrRuO_3$–RuO_2 composite nanofibre mats

Tae-Seon Hyun [a,b], Ho-Gi Kim [b], Il-Doo Kim [a,*]

[a] Center for Energy Materials Research, Korea Institute of Science and Technology, PO Box 131, Cheongryang, Seoul, Republic of Korea
[b] Department of Materials Science and Engineering, Korea Advanced Institute of Science and Technology, Daejeon 305-701, Republic of Korea

ARTICLE INFO

Article history:
Received 8 July 2009
Received in revised form 18 August 2009
Accepted 27 August 2009
Available online 16 September 2009

Keywords:
Nanofibre
Perovskite
Strontium ruthenate
Ruthenium oxide
Electrospinning
Electrochemical capacitor

ABSTRACT

This study reports the facile synthesis of highly conductive $SrRuO_3$(SRO)–RuO_2 composite nanofibre mats and their potential suitability for application in electrochemical capacitors as an active electrode material. SRO–RuO_2/poly(vinyl acetate) composite nanofibre mats are electrospun on to a Au-coated SiO_2/Si substrate and a Ti substrate, subsequently thermocompressed at 60 °C, and calcined at various temperatures (from 350 to 850 °C). The calcined SRO–RuO_2 nanofibre mats exhibit porous morphologies and bundle shapes composed of multiple-fibrils with a nanoparticle diameter ranging from 20 to 50 nm. Single SRO–RuO_2 nanofibre and multiple SRO–RuO_2 nanofibre mats show high electrical conductivity of 476 and 40.8 S cm^{-1}, respectively. Pseudocapacitors using SRO–RuO_2 nanofibre mats calcined at 350 °C exhibit a high specific capacitance of 192 F g^{-1} at a scan rate of 10 mV s^{-1}. The superior capacitance retention (83.4%) of the SRO–RuO_2 nanofibre mats is maintained even at rapid scan rate of 1000 mV s^{-1}.

1. Introduction

One-dimensional (1D) nanomaterials and nanostructures have been intensively investigated due to their unique physical properties and various potential applications [1–3]. In particular, 1D nanostructured metal oxides including nanotubes, nanowires, and nanofibres have been a subject of active research. Moreover, they have been developed extensively from simple binary oxides (SnO_2 [4], TiO_2 [5] and ZnO [6]) to complex oxides ($BaTiO_3$ [7], $BiFeO_3$ [8], TiFeO [9], and Pb(Zr,Ti)O_3 [10]). To date, various nanostructure synthetic and fabrication methods have been proposed [11–13]. Among these methods, electrospinning is one of the simplest, most cost-effective and versatile techniques for creating organic/inorganic nanofibres through a process of utilizing target material precursors and a matrix polymer [14]. Metal oxide nanofibres with a variety of morphologies have been demonstrated by subsequent calcination of electrospun composite nanofibres [15].

$SrRuO_3$ (SRO) has a $GdFeO_3$-type orthorhombic distorted perovskite structure with lattice parameters of $a_0 = 5.53$ Å, $b_0 = 5.57$ Å, and $c_0 = 7.85$ Å. The compound has a pseudo-cubic structure with a unit cell of $a_0 = b_0 = c_0 = 3.93$ Å, $\alpha = \beta = 90°$, $\gamma = 89.6°$ via tilting of the RuO_6 octahedra. This structure results in highly conductive properties with a low resistivity of 275 μΩ cm at room temperature [16]. Based on its excellent metallic properties and structural compatibility with other ferroelectric ($BaTiO_3$ [17], Pb(Zr,Ti)O_3 [18]), paraelectric ($SrTiO_3$ [19], $BaSrTiO_3$ [20]), multiferroic ($BiFeO_3$) [21] and superconducting ($YBa_2Cu_3O_{7-\delta}$) [22] oxides, SRO has been considered as a potential candidate for bottom electrode materials in oxide electronic devices, leading to the improvement of device performance and the minimization of fatigue properties [23–25]. Research on SRO has largely focused on the fabrication of thin films with excellent structural and electrical properties for a suitable bottom electrode of various functional films with a perovskite structure. Electrochemical capacitors using SRO materials have rarely been reported.

So far, a wide variety of synthetic approaches have been developed to improve the specific capacitance and rate capability of electrochemical capacitors by combining conducting nanostructures and hydrous metal oxide coating layers, leading to good electron and proton conductivity. These nanostructures include hydrous RuO_2-coated crystalline RuO_2 vertical nanorods [26] and hydrous RuO_2-coated carbon-nanotubes [27]. These multi-layered nanostructures result in a high specific capacitance in the approximate range of 500–1300 F g^{-1} [26–29]. Although a hydrous RuO_2/crystalline RuO_2 multilayer structure clearly improves the capacitance, the practical fabrication of unique conducting nanostructures without a subsequent coating treatment specially optimized for a pseudocapacitor with a

* Corresponding author. Tel.: +82 2 958 6425; fax: +82 2 958 5309.
E-mail address: idkim@kist.re.kr (I.-D. Kim).

0378-7753/$ – see front matter © 2009 Elsevier B.V. All rights reserved.
doi:10.1016/j.jpowsour.2009.08.103

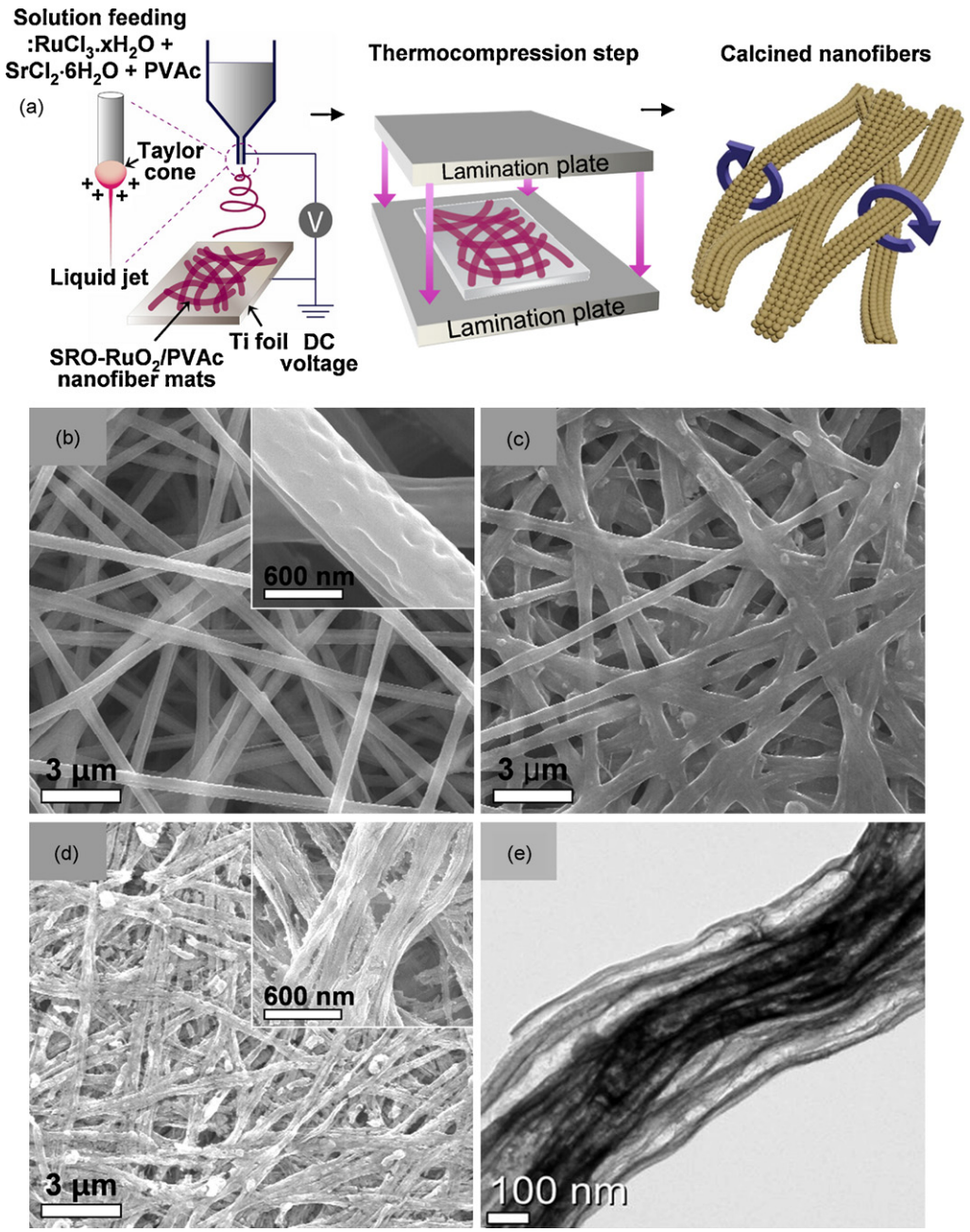

Fig. 1. (a) Procedure of electrospinning, thermocompression and calcinations steps. (b) SEM image of as-spun SRO–RuO_2/PVAc composite nanofibre mats prepared by electrospinning. (c) SEM image of SRO–RuO_2/PVAc composite nanofibre mats after thermocompression at 60 °C for 60 s. (d) SEM image of SRO–RuO_2 nanofibre mats calcined at 350 °C. (e) HR-TEM image of SRO–RuO_2 nanofibre with a fibrilar structure.

high rate capability is difficult to achieve in a single-step process.

This study reports the fabrication of perovskite $SrRuO_3$ nanofibres and potential use in pseudocapacitors of highly conductive SRO–RuO_2 composite nanofibre mats, for the first time, by electrospinning. The microstructure and phase identification of electrospun SRO–RuO_2 composite nanofibre mats are characterized by scanning electron microscopy (SEM), X-ray diffraction (XRD) and high-resolution transmission electron microscopy (HR-TEM). The electrical properties of single SRO–RuO_2 nanofibre and SRO–RuO_2 nanofibre mats are characterized by current–voltage (*I–V*) measurements, and a high power electrochemical capacitor is investigated by means of conducting SRO–RuO_2 nanofibre mats as an active electrode material.

2. Experimental process

2.1. Synthesis of SRO–RuO_2 Nanofibres

The precursor solution for electrospinning was prepared by dissolving ruthenium (III) chloride hydrate ($RuCl_3{\cdot}xH_2O$, Aldrich), strontium (II) chloride hexahydrate ($SrCl_2{\cdot}6H_2O$, Aldrich) and poly(vinyl acetate) (PVAc) (M_W = 1,000,000 g mol^{-1}) in the N,N-dimethylformamide (DMF). In the electrospinning process, the precursor solution was injected through a stainless-steel needle (21 gauge, orifice diameter = 300 μm) that was connected to a high-voltage d.c. power supply (high-voltage power supply series 230, Bertan). The solution was continuously fed through the needle using a syringe pump (KD Scientific, 781200) at a rate of

10 μm min^{-1}. A high voltage (12–15 kV) was applied between the needle and the grounded collector 15 cm below the needle. As a result, a continuous stream of SRO–RuO_2 precursor/PVAc composite nanofibre with a uniform diameter of a few hundred nanometers was ejected from the needle and collected on a titanium plate (99.7%, Aldrich). Subsequently, the as-spun SRO–RuO_2 precursor/PVAc composite fibre mats were thermocompressed for 60 s using preheated metallic plates at 60 °C. Finally, the samples were calcined at temperatures ranging from 350 to 850 °C in air for 30 min.

2.2. Characterization

Scanning electron microscopy (SEM) (FE-SEM, HITACHI S4200) was utilized to observe the development of the microstructure during the process step. X-ray diffraction (XRD) measurements were taken with monochromatic Cu Kα (λ = 1.54 Å) radiation to investigate the phase composition and crystalline structure of the SRO–RuO_2 nanofibre mats at different calcination temperatures. Thermal gravimetric/differential thermal analyses (TG/DTA) (TG2050 thermal analyzer system, Ta instrument, Inc.) were carried out to measure the thermal behaviour of the SRO–RuO_2 precursor/PVAc composite nanofibres. The electrical properties of an individual SRO–RuO_2 nanofibre and of SRO–RuO_2 nanofibre mats were characterized by a current–voltage (*I–V*) test, which was performed with a semiconductor device analyzer (B1500A, Agilent Technologies) in darkness at room temperature (RT).

Electrochemical measurements were performed in a three-electrode system that used the selected SRO–RuO_2 nanofibre mats as a working electrode, a Pt counter electrode, and an Ag|AgCl reference electrode with saturated KCl solution. Cyclic voltammetry was performed using a potentiostat/galvanostat/EIS device (VSP, BioLogic) in aqueous 1 M H_2SO_4 sulfuric acid solution at room temperature. The cyclic voltammograms of the electrodes were recorded at a scan rate of 10–2000 mV s^{-1} over a voltage range of 0–1 V. A sinusoidal potential with an amplitude rating of 10 mV within a frequency range from 500 kHz down to 10 mHz was used in electrochemical impedance spectroscopy (EIS) measurements.

3. Results and discussion

Fig. 1(a) illustrates the procedure, including electrospinning, thermocompression and calcinations steps, which was used to fabricate the SRO–RuO_2 composite nanofibre mats. Fig. 1(b) exhibits FE-SEM images taken of the development of the microstructure while synthesizing the SRO–RuO_2 composite nanofibre mats by electrospinning. As shown in Fig. 1(b), the as-spun SRO–RuO_2/PVAc composite nanofibres exhibited randomly oriented fibres in the form of nonwoven mats with a range of 500–600 nm. Following the electrospinning process, a thermocompression process was undertaken to improve the adhesion between the nanofibre mats and the Ti substrate. The advantages of this process can be found in the literature [5,6]. SRO–RuO_2/PVAc composite nanofibre mats thermocompressed at 60 °C above the T_g (glass transition temperature) of PVAc (28–30 °C) have an interconnected morphology, as illustrated in Fig. 1(c), due to the partial melting of the PVAc that results in remarkably improved adhesion. By contrast, nanofibre mats calcined without a thermocompression step cracked and peeled off from the substrates. Following the thermocompression process, the specimen was calcined to remove the polymer template by thermal decomposition of the organic components and to crystallize the SRO–RuO_2 nanofibres.

Fig. 1(d) presents an FE-SEM image of the SRO–RuO_2 nanofibre mats after calcination at 350 °C. Calcined SRO–RuO_2 nanofibre mats exhibit porous morphologies with high surface-to-volume ratios. In particular, significant differences are observed in the microstructures of the SRO–RuO_2 mats with variation in the calcination temperatures. The particle (grain) size comprising the SRO–RuO_2 nanofibre mats increases with increase in the calcination temperature, leading to more porous microstructures (not shown). These variations were caused by the phase transition of the SRO, which further crystallizes in the temperature range of 450–850 °C to form a perovskite structure. Nanofibre mats calcined at lower temperatures ranging from 350 to 650 °C are found to be a mixture of the perovskite SRO and rutile RuO_2 phases. It is important to note that SRO–RuO_2 composite nanofibre mats are composed of multiple-fibrils with diameters ranging from 20 to 50 nm, as shown in the inset of Fig. 1(d). The fibrils, consisting of nanoparticles of less than 5 nm, are sparsely agglomerated within individual bundles. The formation mechanism of the fibrilar structure can be attributed to the following procedures. The precursor solution is divided into SRO–RuO_2-rich and PVAc-rich domains through phase separation in the sol–gel reaction. During the electrospinning process, their domain causes elongation and thereby forms the fibrils. Subsequently, the fibrilar structure of SRO–RuO_2 is formed by the removal of PVAc during the calcination process [30]. These fibrils offer high porosity for efficient permeability of electrolyte into the inner fibrils while maintaining a high surface area for enhanced surface activity. To examine the microstructure of the SRO–RuO_2 fibrils, high-resolution transmission electron microscopy (HR-TEM) characterizations were conducted.

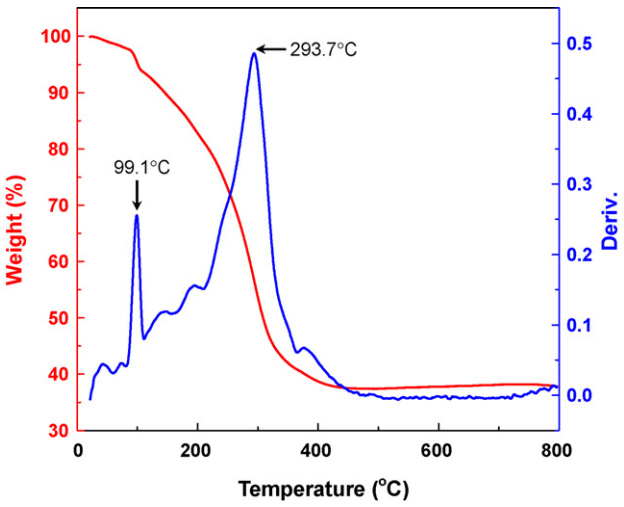

Fig. 2. Thermogravimetric analysis (TGA) and differential thermal analysis (DTA) of SRO–RuO_2 nanofibre mats in 20–800 °C temperature range with a heating rate of 10 °C min^{-1}.

Fig. 1(e) shows a representative TEM micrograph of the SRO–RuO_2 fibrils. Fibrils consisting of nanoparticles of less than 5 nm are clearly visible in the HR-TEM image. TGA and DTA measurements were carried out at a heating rate of 10 °C min^{-1} over a temperature range of 20–800 °C. The TGA curve exhibits three distinct stages of weight loss, as shown in Fig. 2. The first stage commences at a temperature of 80 °C due to the evaporation of water and residual solvent, i.e., DMF. The second weight-loss stage over a broad temperature range from 110 to 400 °C (with the centre of the peak at 293.7 °C) is due to degradation of the PVAc, the evolution of chlorine gas from the precursor, and the crystallization of the SRO and RuO_2 phases. The temperature plateau curves without a loss of weight indicate the formation of crystalline SRO and RuO_2 above 400 °C.

Structural identification of the electrospun SRO–RuO_2 composite nanofibre mats, calcined at various temperatures from 350 to 850 °C were investigated by means of XRD analysis in a 2θ range of 20° and 60°. As shown in Fig. 3, the XRD patterns of

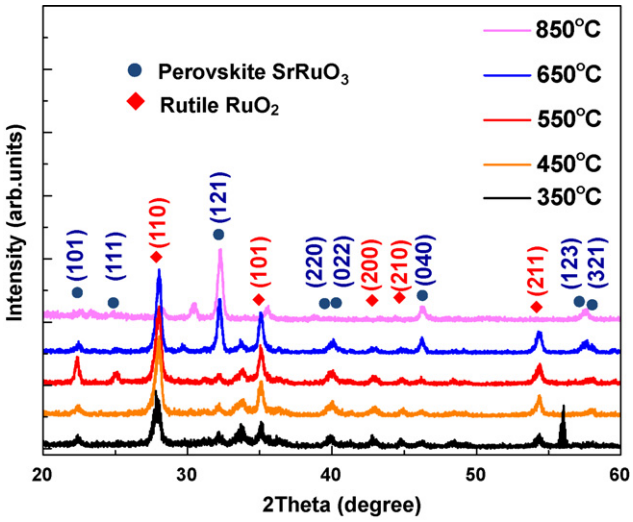

Fig. 3. X-ray diffraction pattern of SRO–RuO_2 nanofibre mats calcined at 350, 450, 550, 650 and 850 °C for 30 min.

SRO–RuO_2 nanofibre mats calcined at temperatures above 350 °C display mixed polycrystalline diffraction peaks of the rutile RuO_2 phase characterized with primary (1 0 1), (1 1 0) and (2 1 1) peaks (corresponding to PDF 43-1027) and diffraction peaks of crystalline $SrRuO_3$, i.e., diffraction peaks at $2\theta = 22.61°$, 25.32°, 32.20°, 42.95°, 43.10°, 46.18°, 57.30°, and 57.53°, which are assigned to the (1 0 1), (1 1 1), (1 2 1), (2 2 1), (1 2 2), (0 4 0), (3 2 1) and (1 2 3) planes of the JCPDS 43-0472 specification. The crystallinity of the rutile RuO_2 phase and perovskite SRO phase increase as the calcination temperature is increased. When the calcination temperature exceeds 650 °C, the SRO diffraction peaks of the (1 2 1) and (0 4 0) planes placed at $2\theta = 32.20°$ and 46.18° are clearly observed. This result indicates that nanoparticles of the RuO_2 and SRO phases coexist in the nanofibre mats. It is possible to obtain a well-crystallized $SrRuO_3$ perovskite structure at a calcination temperature of 850 °C.

In order to investigate the microstructure of the SRO–RuO_2 nanofibre mats, HR-TEM analysis was conducted. SRO–RuO_2 nanofibre mats calcined at a temperature of 350 °C have a highly porous and nonwoven structure, as indicated in Fig. 4(a). In the magnified TEM image of the SRO–RuO_2 nanofibre mats (see Fig. 4(b)), partial crystalline nanoparticles of a size less than 5 nm are clearly visible in SRO–RuO_2 fibrilar structure. The weak spots of the selected area electron diffraction (SAED) pattern, as shown in the inset of Fig. 4(b), are evidence of the existence of small nanopar-

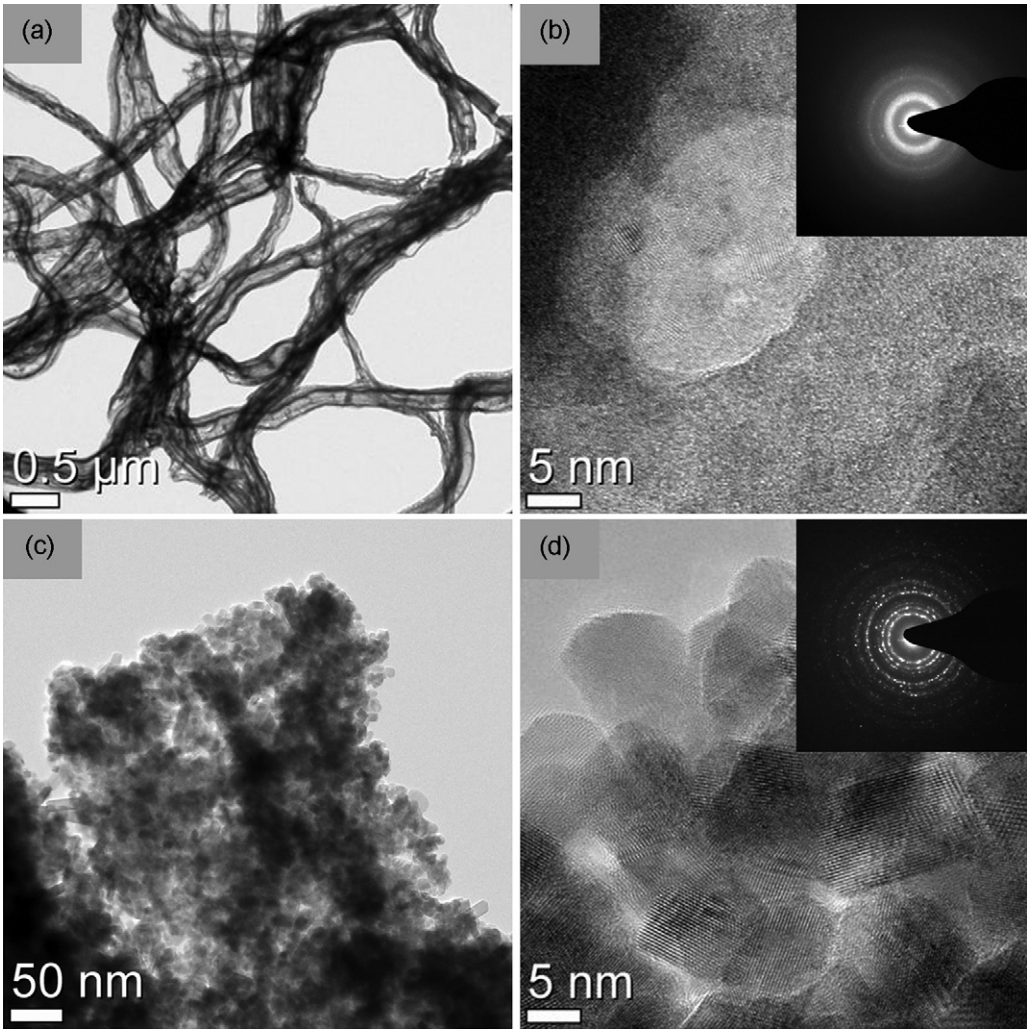

Fig. 4. (a) HR-TEM image of SRO–RuO_2 nanofibre mats. (b) HR-TEM image of RuO_2 nanograins calcined at 350 °C. Inset shows selected area electron diffraction (SAED) pattern of SRO–RuO_2 nanograins. (c) HR-TEM image of SRO–RuO_2 nanofibre mats. (d) HR-TEM image of SRO–RuO_2 nanograins calcined at 650 °C. Inset shows selected area electron diffraction (SAED) pattern of SRO–RuO_2 nanograins.

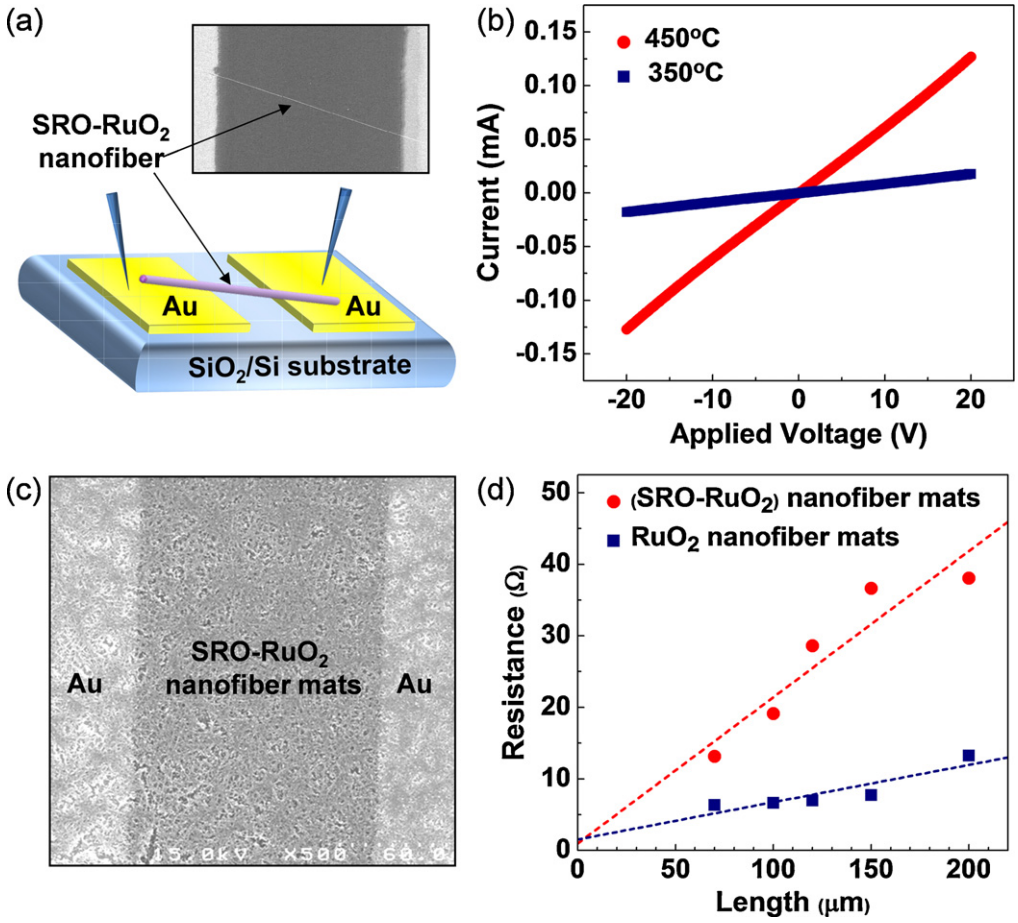

Fig. 5. (a) FE-SEM image and schematic diagram of an electrode of single SRO–RuO_2 nanofibre on a Au electrode patterned on a SiO_2/Si substrate for *I–V* curve measurement. (b) *I–V* curve of single SRO–RuO_2 nanofibre calcined at 350 and 450 °C. (c) SEM image of the SRO–RuO_2 nanofibre mats on Au electrodes patterned on top of a SiO_2/Si substrate. (d) *I–V* curves of SRO–RuO_2 nanofibre mats and RuO_2 nanofibre mats calcined at 350 °C.

ticles. In the case of SRO–RuO_2 nanofibre mats calcined at 650 °C, nanoparticles with an average size of 10 nm can be observed due to the grain growth caused by the high temperature calcination. The lattice fringes of individual nanoparticles are well characterized in Fig. 4(d). The SAED pattern of the SRO–RuO_2 nanofibre mats calcined at 650 °C presents distinct ring patterns composed of sharp spots. In particular, the two phases of perovskite SRO and rutile RuO_2 coexist in HR-TEM images.

The electrical properties of SRO–RuO_2 composite nanofibres synthesized by electrospinning were characterized by two-probe *I–V* measurements. In order to characterize the electrical conductivity, Au electrodes were patterned on top of SiO_2/Si substrates with the aid of a shadow mask. The line width of each Au electrode was 2000 μm spaced 70–200 μm apart, as shown in the SEM micrograph in Fig. 5(a) and (c). The electrical conductivity values of a single SRO–RuO_2 nanofibre and multiple SRO–RuO_2 nanofibre mats were estimated from the equation, $\sigma = l/RA$, where R is the resistance, A is the cross-sectional area ($A = \pi ab$ for a single SRO–RuO_2 fibre, with a the width and b the height of a single SRO–RuO_2 fibre), and l denotes the distance between the electrodes. The *I–V* profile of an individual SRO–RuO_2 nanofibre shows a linear relationship, which confirms the ohmic behaviours between the SRO–RuO_2 nanofibre and the Au electrodes. A single SRO–RuO_2 nanofibre calcined at 350 and 450 °C shows conductivity values of 2.39×10^1 and 4.76×10^2 S cm^{-1}, respectively. It is found that the conductivity increases as the calcination temperature is increased due to the enhanced crystallinity and the growth of the crystalline size comprising the SRO–RuO_2 nanofibre mats. A similar electrical behaviour was observed for multiple SRO–RuO_2 nanofibre mats. In order to investigate the electrical conductivity and contact resistance characteristics of SRO–RuO_2 nanofibre mats, the transfer line method (TLM) was used. Fig. 5(d) exhibits the resistance characteristics while varying the contact spacing (L) between both gold electrodes in a range from 70 to 200 μm. The total resistance (R_T) as a function of the distance (L) is given by the following equation: $R_T = R_S L/W + 2R_C$, where R_S is the sheet resistance, W is the width of the electrode (0.2 cm), and R_C is the contact resistance. According to the aforementioned equation, R_C can be calculated as the half of the intercept value, and R_S can be determined from the slope of the line between R_T and L. The measured values of the contact resistance and the sheet resistance of the SRO–RuO_2 nanofibre mats are 0.49 Ω and 408.7 Ω □$^{-1}$, respectively. The specific contact resistance (ρ_C) calculated from $\rho_C = R_C^2 W^2/R_S$ is 2.35×10^{-5} Ω cm^2. The electrical conductivity of the SRO–RuO_2 nanofibre mats calcined at 350 °C is 4.08×10^1 S cm^{-1}, a value that is comparable with that of a single SRO–RuO_2 nanofibre. This conductivity is one order of magnitude lower than the conductivity value (2.74×10^2 S cm^{-1}) of electrospun RuO_2 nanofibre mats calcined at 350 °C, as shown in Fig. 5(d). This result is due to the low crystallinity and lower conductivity of the SRO phase as compared with the RuO_2 phase. A conductivity of 4.08×10^1 S cm^{-1} is still high enough to transport electrons rapidly, leading to a high rate capability of the electrochemical capacitor.

The electrochemical characteristics of the electrode using the SRO–RuO_2 nanofibre mats were investigated through cyclic voltammetry at a scan rate ranging from 10 to 1000 mV s^{-1} over a potential range of 0–1.0 V with respect to a Ag|AgCl electrode

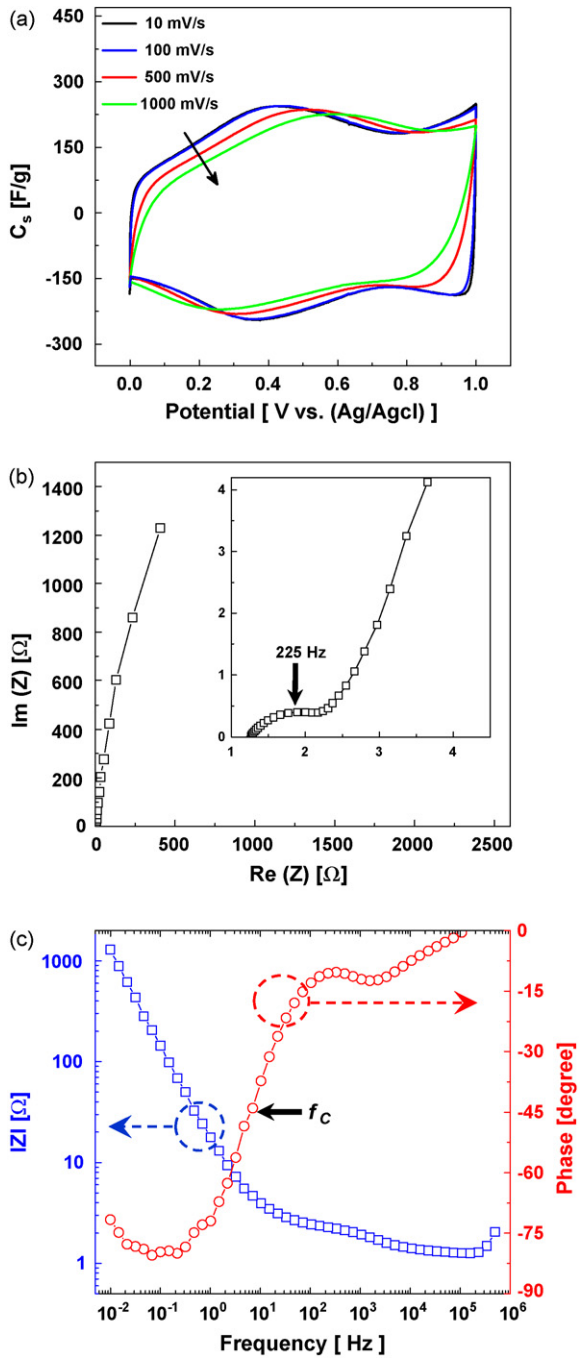

Fig. 6. (a) Cyclic voltammograms result at various scan rates of 10, 100, 500, and 1000 mV s^{-1}. (b) Nyquist plot and (c) Bode plots of an electrode of SRO–RuO_2 nanofibre mats calcined at 350 °C.

using 1 M H_2SO_4 as an electrolyte. The cyclic voltammogram of SRO–RuO_2 nanofibre mats has a rectangular shape, which indicates good pseudocapacitive behaviour for an electrochemical capacitor performance up to a rapid scan rate of 1000 mV s^{-1}, as indicated in Fig. 6(a). The specific capacitance values were calculated from the cyclic voltammogram curve using the following relationship: $C_{sp} = i/\nu w$, where i is the average current, ν is the scan rate, and w is the weight of the SRO–RuO_2 nanofibre mats (this sample: 0.13 mg). The maximum specific capacitance of the SRO–RuO_2 nanofibre mats calcined at 350 °C is 192.0 F g^{-1} at a scan rate of 10 mV s^{-1}. The specific capacitance is five times higher than that of the electrode using the RuO_2 nanofibre mat calcined at the same temperature of 350 °C (34.5 F g^{-1}) (data not shown). The capacitive responses in the SRO–RuO_2 composite nanofibre mats and in the RuO_2 nanofibre mats both arise from the Faradaic reaction of a proton in the open surface due to the macropores between the nanofibres and the mesopores between the nanoparticles. However, the SRO–RuO_2 nanofibre mats have a non-crystallized region due to the higher crystallization temperature of $SrRuO_3$, while the RuO_2 nanofibre mats are composed of rigid crystalline particles without water contents. In general, anhydrous RuO_2 annealed at temperatures in excess of 350 °C shows a low specific capacitance because the effective thickness for diffusing the proton into the surface of the crystalline component is limited. Thus, SRO–RuO_2 nanofibre mats can offer greatly enhanced accessibility of a proton into the SRO–RuO_2 structure through the amorphous SRO phases, leading to easier proton diffusion into SRO–RuO_2 structures. Indeed, a superior capacitive retention capability is obtained in the electrode using SRO–RuO_2 nanofibre mats. A high specific capacitance of 159.8 F g^{-1} is maintained, even at a scan rate of 1000 mV s^{-1}. The capacitance retention rate of the SRO–RuO_2 nanofibre mats is 83.4% of the maximum capacitance value measured at a scan rate of 10 mV s^{-1}. Zheng [31] reported that the capacitance at higher rates rapidly decreases due to proton depletion and over-saturation in the electrolyte during the charge–discharge response. The excellent rate capability of the SRO–RuO_2 nanofibre mats is closely related to the open structure of the nanofibres, i.e., the effective access of the proton into the active sites as well as the fast electron transport characteristics of conducting SRO–RuO_2 phase.

In order to investigate the charge–discharge properties of the SRO–RuO_2 nanofibre mats, an EIS analysis was conducted over a frequency range of 500 kHz–10 mHz at an a.c. amplitude of 10 mV using a three-electrode configuration cell. The impedance spectrum for the pseudocapacitance response is divided into the three regions of high-, medium- and low-frequency regions according to the main reactions. The high-frequency region is dominated by the charge-transfer process at the surface of the electrode in contact with the electrolyte. The medium-frequency region is diffusion-controlled, and the distributed capacitance and resistance within the film dominate the impedance. In the low-frequency region, non-homogeneous diffusion in the less-accessible sites governs the impedance [32]. The Nyquist plot for the SRO–RuO_2 nanofibre mats shows a vertical line that is nearly parallel to the imaginary axis. It is considered to represent the capacitive behaviour. As shown in the inset of Fig. 6(b), however, a depressed semicircle characterizing the charge-transfer process is revealed in the magnified view of the high-frequency region. The high-frequency region above 225 Hz is defined by a knee frequency which is the lower limit of the high-frequency region. This result is in good agreement with the high-frequency region in the Bode plot of Fig. 6(c). In the low-frequency region, the ideal capacitive behaviour is represented by a capacitor response frequency where the phase angle φ is −45°. The capacitor response frequency (f_C) for the SRO–RuO_2 nanofibre mats is 7 Hz. The capacitor response time (τ_C) is defined as the inverse of f_C. It characterizes the charge–discharge rate for the pseudocapacitor. Therefore, the capacitor response time for the SRO–RuO_2 nanofibre mats is characterized as 0.14 s.

4. Conclusions

Highly porous SRO–RuO_2 composite nanofibre mats are prepared using an electrospinning method. The mats are composed of nanofibrils which consist of nanoparticles. Electrospun SRO–RuO_2 nanofibre mats have a fast pathway of electrons due to the high conductivity of metallic oxide and exhibit facile transfer characteristics of protons due to the existence of amorphous phases. Psuedocapacitor electrodes have been assembled using SRO–RuO_2 nanofibre mats as an active material. The electrochemical performance of the

SRO–RuO_2 nanofibre mats calcined at 350 °C exhibit a high specific capacitance of 192 $F g^{-1}$ at a scan rate of 10 $mV s^{-1}$. Additionally, the capacitance effectively maintained is 83.7% at a high scan rate of 1000 $mV s^{-1}$ due to the open structure of the nanofibrils and the fast electron and proton transfer characteristics of the highly conductive SRO–RuO_2 electrode.

Acknowledgment

This research was supported by a KIST research program under Grant No. 2E21400.

References

[1] Y. Xia, P. Yang, Y. Sun, Y. Wu, B. Mayers, B. Gates, Y. Yin, F. Kim, H. Yan, Adv. Mater. 15 (2003) 353–389.
[2] Y. Huang, X. Duan, Q. Wei, C.M. Lieber, Science 291 (2001) 630–633.
[3] C. Burda, X. Chen, R. Narayanan, M.A. El-Sayed, Chem. Rev. 105 (2005) 1025–1102.
[4] Z.R. Dai, J.L. Gole, J.D. Stout, Z.L. Wang, J. Phys. Chem. B 106 (2002) 1274–1279.
[5] I.D. Kim, A. Rothschild, B.H. Lee, D.Y. Kim, S.M. Jo, H.L. Tuller, Nano Lett. 6 (2006) 2009–2013.
[6] I.D. Kim, J.M. Hong, B.H. Lee, D.Y. Kim, E.K. Jeon, D.K. Choi, D.J. Yang, Appl. Phys. Lett. 91 (2007) 163109.
[7] J. Feenstra, H.A. Sodano, J. Appl. Phys. 103 (2008) 124108.
[8] S.H. Xie, J.Y. Li, R. Proksch, Y.M. Liu, Y.C. Zhou, Y.Y. Liu, Y. Ou, L.N. Lan, Y. Qiao, Appl. Phys. Lett. 93 (2008) 222904.
[9] G.K. Mor, H.E. Prakasam, O.K. Varghese, K. Shankar, C.A. Grimes, Nano Lett. 7 (2007) 2356–2364.
[10] S. Xu, Y. Shi, S.G. Kim, Nanotechnology 17 (2006) 4497–4501.
[11] D. Li, Y. Wang, Y. Xia, Nano Lett. 3 (2003) 1167–1171.
[12] M. Law, J. Goldberger, P. Yang, Annu. Rev. Mater. Res. 34 (2004) 83–122.
[13] M.S. Gudiksen, L.J. Lauhon, J. Wang, D.C. Smith, C.M. Lieber, Nature 415 (2002) 617–620.
[14] I.S. Chronakis, J. Mater. Process. Technol. 167 (2005) 283–293.
[15] R. Ramaseshan, S. Sundarrajan, R. Jose, S. Ramakrishna, J. Appl. Phys. 102 (2007) 111101.
[16] C.B. Eom, R.J. Cava, R.M. Fleming, J.M. Philips, R.B. van Dover, J.H. Marshall, J.W.P. Hsu, J.J. Krajewski, W.F. Peck Jr., Science 258 (1992) 1766–1769.
[17] N.A. Pertsev, A. Petraru, H. Kohlstedt, R. Waser, I.K. Bdikin, D. Kiselev, A.L. Kholkin, Nanotechnology 19 (2008) 375703.
[18] H. Han, R. Ji, Y.J. Park, S.K. Lee, G.L. Rhun, M. Alexe, K. Nielsch, D. Hesse, U. Gösele, S. Baik, Nanotechnology 20 (2009) 015301.
[19] Q. Gan, R.A. Rao, C.B. Eom, J.L. Garrett, M. Lee, Appl. Phys. Lett. 72 (1998) 978–980.
[20] T. Yamada, V.O. Sherman, A. Nöth, P. Muralt, A.K. Tagantsev, N. Setter, Appl. Phys. Lett. 89 (2006) 032905.
[21] R.Y. Zheng, C.H. Sim, J. Wan, J. Am. Ceram. Soc. 91 (2008) 3240–3244.
[22] Q.X. Jia, S.R. Foltyn, P.N. Arendt, J.R. Groves, T.G. Holesinger, M.E. Hawley, P. Lu, Appl. Phys. Lett. 81 (2002) 4571–4573.
[23] P.J. Schorn, D. Bräuhaus, U. Böttger, R. Waser, G. Beitel, N. Nagel, R. Bruchhaus, J. Appl. Phys. 99 (2006) 114104.
[24] H. Miyazaki, Y. Miwa, H. Suzuki, Mater. Sci. Eng. B 136 (2007) 203–206.
[25] S. Kim, J. Koo, S. Shin, Y. Park, Appl. Phys. Lett. 87 (2005) 212910.
[26] D. Susanti, D.-S. Tsai, Y.-S. Huang, A. Korotcov, W.-H. Chung, J. Phys. Chem. C 111 (2007) 9530–9537.
[27] J.-S. Ye, H.F. Cui, X. Liu, T.M. Lim, W.-D. Zhang, F.-S. Sheu, Small 1 (2005) 560–565.
[28] J.P. Zheng, P.J. Cygan, T.R. Jow, J. Electrochem. Soc. 142 (1995) 2699–2703.
[29] C.-C. Hu, K.H. Chang, M.C. Lin, Y.T. Wu, Nano Lett. 6 (2006) 2690–2695.
[30] S.M. Jo, M.Y. Song, Y.R. Ahn, C.R. Park, D.Y. Kim, J. Macromol. Sci. A 42 (2005) 1529–1540.
[31] J.P. Zheng, Electrochem. Solid-State Lett. 2 (1999) 359–361.
[32] W. Sugimoto, K. Yokoshima, Y. Murakami, Y. Takasu, Electrochim. Acta 52 (2006) 1742–1748.